Fast loaded dual species magneto optical trap of cold sodium and potassium atoms with light-assisted inter-species interaction

Cite as: AIP Advances 13, 065317 (2023); doi: 10.1063/5.0154985
Submitted: 17 April 2023 • Accepted: 23 May 2023 •
Published Online: 8 June 2023

Sagar Sutradhar, Anirban Misra, Gourab Pal, Sayari Majumder, Sanjukta Roy, and Saptarishi Chaudhuri[a)]

AFFILIATIONS

Raman Research Institute, C. V. Raman Avenue, Sadashivanagar, Bangalore 560080, India

[a)]Author to whom correspondence should be addressed: srishic@rri.res.in

ABSTRACT

We present the design, implementation, and detailed experimental characterization and comparison with numerical simulations of two-dimensional magneto-optical traps (MOTs) of bosonic ^{23}Na and ^{39}K atoms for loading the cold atomic mixture in a dual-species 3DMOT with a large number of atoms. We report our various measurements pertaining to the characterization of two 2D$^+$MOTs via the capture rate in the 3DMOT and also present the optimized parameters for the best performance of the system of the cold atomic mixture. Under the optimized condition, we capture more than 3×10^{10} ^{39}K atoms and 5.8×10^8 ^{23}Na atoms in the 3DMOT simultaneously from individual 2D$^+$MOTs with a capture rate of 5×10^{10} and 3.5×10^8 atoms/sec for ^{39}K and ^{23}Na, respectively. We also demonstrate improvements of more than a factor of 5 in the capture rate in the 3DMOT from the cold atomic sources when a relatively high-power ultraviolet light is used to cause light-induced atomic desorption in the 2D$^+$MOT glass cells. A detailed study of the light assisted interspecies cold collisions between the co-trapped atoms is presented, and interspecies loss coefficients have been determined to be $\beta_{NaK} \sim 2 \times 10^{-12}$ cm^3/sec. The cold atomic mixture would be useful for further experiments on quantum simulation with ultra-cold quantum mixtures in optical potentials.

I. INTRODUCTION

Ultra-cold quantum gases in optical potentials offer a versatile platform for quantum simulation,[1–5] precision measurements,[6] and quantum technologies[7] due to the high degree of controllability of such systems such as inter-atomic interaction, dimensionality, spin states, and external potentials. This makes ultra-cold atomic ensembles an ideal "quantum toolbox," leading to unprecedented progress in this research field.

Quantum gas mixtures with dual atomic species have attracted considerable interest since they offer a wealth of novel possibilities. Quantum degenerate mixtures realized by using single atomic species in different Zeeman sub-levels,[8–10] multiple isotopes of the same species, or different atomic species[11–26] can be used to investigate novel quantum phases hitherto unexplored in single atomic species. For example, the physics of impurities coupled with degenerate gas[27–29] is of fundamental importance in condensed matter systems. Novel exotic quantum phases such as quantum droplets in a spin mixture of Bose gases were recently proposed[30] and observed in homo- and hetero-nuclear quantum mixtures.[31–33] Quantum mixtures can also be used to create hetero-nuclear stable polar molecules,[34–36] which is useful to study controlled ultra-cold chemistry[37] as well as long-range anisotropic dipolar interactions.[38–41]

A quantum degenerate mixture of sodium and potassium is an attractive combination for a hetero-nuclear quantum mixture experiment. Both the Bose–Bose mixture (^{23}Na–^{39}K and ^{23}Na–^{41}K) and Bose–Fermi mixture (^{23}Na–^{40}K) can be obtained, opening up a myriad of possibilities for exploring the many-body physics arising due to the interplay between inter-species and intra-species interaction, with quantum statistics playing a significant role. Another important advantage of the combination of sodium and potassium for

the hetero-nuclear quantum mixture is that the Na–K ground-state polar molecules[42,43] are chemically stable compared to other combinations of inter-species hetero-nuclear molecules, with a large dipole moment of ~2.72 Debye paving the way to exploring long-range dipolar interaction for quantum simulation.[44]

In this article, we describe our experimental setup to realize an ultra-cold atomic mixture of ^{23}Na and ^{39}K atoms in a dual-species magneto-optical trap (3DMOT) loaded from cold atomic beams produced via two independent, compact, and efficient two-dimensional magneto-optical traps (2D$^+$MOTs) of ^{23}Na and ^{39}K. We also present the detailed characterization of the performance of the cold atom sources of both ^{23}Na and ^{39}K atoms to obtain the optimized experimental parameters for the best possible performance of the cold atomic beam sources.

The various sections in this article are organized as follows: In Sec. II, we provide a detailed description of the experimental system including the ultra-high vacuum assembly and laser systems. In Sec. III, we focus on the characterization and performance of the cold atomic beam sources. In Sec. IV, we give a detailed theoretical description of the numerical simulations performed in order to compare with the experimental results of the atomic sources. We have provided a complete system performance study in Sec. V. Finally, we discuss the interspecies light-assisted collisions between hetero-nuclear cold atoms in Sec. VI.

II. EXPERIMENTAL SETUP

In this experimental setup, a large number of ^{23}Na and ^{39}K atoms are simultaneously captured in a dual-species 3DMOT from two independent sources of cold atomic beams. There are stringent requirements for the design of the apparatus, such as good optical access for trapping laser beams as well as detection, ultra-high vacuum to ensure longer trap lifetime of the atoms, and a high magnetic field gradient for magnetic trapping. Our experimental setup is designed and built to fulfill these requirements and enables further experiments on the quantum degenerate mixture in both magnetic and optical potentials.

The conflicting requirements of having a large number of atoms for experiments on degenerate quantum gases as well as a long lifetime of the atomic cloud have led to the design of multi-chamber vacuum systems for such experiments where the MOT is loaded from a cold atomic beam source instead of the background vapor. Examples of such cold atomic beam sources are the Zeeman slower,[45] low velocity intense source,[46] 2DMOT,[47] 2D$^+$MOT,[48,49] and pyramidal MOT.[50] Among such possibilities, the 2D$^+$MOT offers the most compact design with the most efficient performance. For ^{23}Na and ^{39}K atoms, Zeeman slowers[45,51,52] and 2DMOTs[52–55] have been realized. In the case of a hetero-nuclear atomic species mixture, to the best of our knowledge, our experiment is the first demonstration where both the atomic species are simultaneously derived from compact 2D$^+$MOT configurations.

A. Vacuum assembly

A schematic view of our vacuum system is shown in Fig. 1. A spherical octagon-shaped chamber for the 3DMOT, made with non-magnetic stainless steel (Kimball Physics-MCF600-SphOct-F2C8) placed at the center of the vacuum manifold, is attached with two independent 2D$^+$MOT glass cells (Precision Glassblowing, CO, USA). For both ^{23}Na and ^{39}K atoms, the vacuum chamber of the 2D$^+$MOT consists of a cuboidal glass cell (dimensions 85 × 40 × 40 mm^3), whose longitudinal axis is aligned horizontally and placed along the axis of a differential pumping tube connecting the 2D$^+$MOT glass cell and the 3DMOT chamber. The atomic beam is prepared along the longitudinal axis of the glass cell. The differential pumping tube was made from a single block of oxygen-free highly conductive (OFHC) copper. One end of the tube is a 45°-angled polished mirror with a round surface of a diameter of 18 mm and placed inside the glass cell. The other end of the tube has a disk

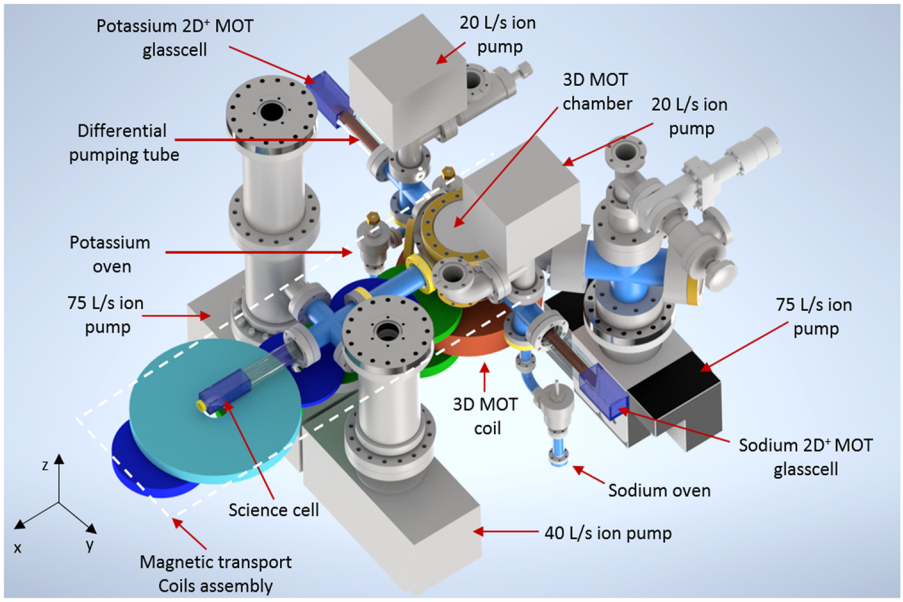

FIG. 1. Schematic of the vacuum assembly. The two-species MOT is loaded from two independent 2D$^+$MOTs as sources of cold ^{23}Na and ^{39}K atoms. The dual-species 3DMOT is produced in a spherical octagonal chamber. The UHV side is pumped by three large-capacity ion pumps whereas the two independent source regions are pumped with two 20 l/s ion pumps. Coils made of hollow-cored water-cooled copper tubes placed outside the 3DMOT chamber are used to generate the quadrupole magnetic field for trapping of atoms. A single-arm magnetic transport allows transferring the cloud to the "science cell" with large optical access.

shape of a diameter of ≈ 48 mm and a thickness of 10 mm. This disk acts as a gasket between the two CF40 flanges of the 2D$^+$MOT and the 3DMOT chamber. The 45° surface of the copper tube allows the alignment of the longitudinal cooling laser beams, as described later in this article.

The differential tube has a hole that originates at the center of the 45° surface and runs along the axis of the tube and ends up at the UHV side of the 3DMOT chamber. The differential pumping hole starts with a diameter of 2 mm and then widens up in two steps over a total distance of 270 mm. The hole reaches a diameter of 8 mm (6 mm) after the first 20 mm length and subsequently widens up to 14 mm (12 mm) after the next 120 mm length for ^{23}Na (^{39}K) tubes.

The differential pumping tube has a conductance of 0.043 l/s (0.038 l/s) for the ^{23}Na (^{39}K) side. The two 2D$^+$MOT glass cells are individually pumped using two 20 l/s ion pumps. The 3D-MOT chamber is pumped by a 75 l/s ion pump, and the generated pressure ratio between the two chambers is 1200 (1400) for the ^{23}Na (^{39}K) side.

In addition, our experimental system includes a magnetic transport tube and a glass cell ("science cell") of a dimension of 85 × 30 × 30 mm^3 pumped by two more ion pumps with 40 and 75 l/s pumping speeds. We also occasionally use a titanium sublimation pump to maintain the base pressure below 10^{-11} mbar near the "science cell." The base pressure near the 3DMOT chamber is measured using an ionization gauge to be ~7×10^{-11} mbar, which is also consistent with our observed cold atom trap lifetime of ~48 s. On the other hand, both the 2D$^+$MOT glass cells are maintained at a base pressure below 10^{-9} mbar.

We have used a natural abundance source (ingot) of sodium [Sigma-Aldrich (262714-5G)]. The ingot is placed inside a CF16 full nipple and attached to the glass cell through a CF16 angle gate valve (MDC Vacuum). Heating tapes are wrapped around the full nipple and the gate valve in such a way that a temperature gradient could be maintained from the oven toward the glass cell, which ensures that the sodium drifts into the cell and remains there. The purpose of the gate valve is two-fold. First, it determines the amount of flow of sodium vapor into the glass cell, and second, during replenishment of the source, it would allow us to isolate the oven from the rest of the vacuum system.

We have also used a natural abundance source (ingot) of potassium from Sigma-Aldrich (244856-5G) as the source for loading atoms into the ^{39}K 2D$^+$MOT. The design of the potassium oven is similar to the sodium one. Here, we have kept natural abundance potassium and enriched ^{40}K (10% enrichment from Precision Glassblowing, USA) inside two different CF-16 full nipples, followed by respective CF-16 angle gate valves. These two ovens are connected and integrated with the 2D$^+$MOT glass cell.

B. Laser systems

The cooling and repumping beams for laser cooling of sodium atoms were derived from a frequency-doubled diode laser system (Toptica TA-SHG pro), which typically gives a total output power of 1100 mW at 589 nm (^{23}Na D2 transition). The laser beam from the TA-SHG pro is divided into several beams. A low-power beam (typically 5 mW) is fed into an acousto-optic modulator (AOM) (AA Optics, center frequency of 110 MHz) double-pass assembly and subsequently directed into the saturation absorption spectroscopy (SAS) setup. The spectroscopy for sodium is realized using a vapor cell of 75 cm length from Triad Technologies (TT-NA-75-V-P), which is heated to 150 °C to create a sufficiently high vapor pressure for absorption.

The cooling beams for the 2D$^+$MOT as well as the 3DMOT are generated using two independent AOM (Isomet 110 MHz) double-pass setups and tuned appropriately (red-detuned) from the $3^2S_{1/2}|F=2\rangle \rightarrow 3^2P_{3/2}|F'=3\rangle$ transition. The repumping beams are tuned in resonance with the transition $3^2S_{1/2}|F=1\rangle \rightarrow 3^2P_{3/2}|F'=2\rangle$, bypassing the cooling beams through two independent electro-optic modulators (EOM) (QuBig-EO-Na1.7M3). The EOMs are powered by two independent drivers (QuBig-E3.93KC), and each sideband has typically 20% of the power of the carrier (cooling) frequency. The co-propagating cooling and repumping beams are injected into their respective polarization-maintaining (PM) fibers and transferred to the experimental optical table for the realization of the 2D$^+$MOT and the 3DMOT.

For potassium atoms, we use two independent External Cavity Diode Lasers (ECDLs) from Toptica Photonics for deriving the cooling (DL pro) and repumping (DL 100) laser beams. Each of these laser outputs is amplified using two independent tapered amplifiers (Toptica BoosTA pro), with the maximum output power reaching 2 W. The output of each of the potassium lasers is divided into two beams. The one with a low power of ≈5 mW is fed into the SAS setup. The spectroscopy is realized with a glass vapor cell of 5 cm length, in which a K-sample with natural abundance is heated to 50 °C. The other output beams from the two potassium lasers are injected into the Tapered Amplifiers (TAs). The amplified output beams of the TAs are split into several beams and sent through the corresponding AOM (AA Optics, 200 MHz) double pass configurations to prepare the beams at appropriate frequencies to be used as the cooling and repumping beams for the 2D$^+$MOT and the 3DMOT. The K- cooling laser is offset-locked to the $4S_{1/2}|F=2\rangle \rightarrow 4P_{3/2}|F'=3\rangle$ transition of ^{39}K atoms, while the repumping laser is locked to the $4S_{1/2}(|F=1\rangle, |F=2\rangle) \rightarrow 4P_{3/2}$ crossover transition.

The laser beams transferred to the main experimental table using PM fibers (Schafter+Kirchhoff GmbH) are out-coupled by the corresponding fiber-collimators, which provides a collimated Gaussian beam of $1/e^2$ diameter of 12 mm.

III. ATOMIC BEAM SOURCE

The 3DMOT can be loaded efficiently from a cold atomic beam with a high capture rate of atoms. The preparation of an atomic beam requires high atomic vapor pressure (in the range of 10^{-8}–10^{-6} mbar). Generally, it is prepared in a section spatially separated from the 3DMOT section (which requires a UHV environment). The atomic beam is directed through a differential pumping tube into the 3DMOT section, which maintains a pressure difference of a few orders of magnitude between the 2D$^+$MOT region and the UHV 3DMOT region. This atom loading scheme not only keeps the 3DMOT in the UHV range to minimize the collisions with the room-temperature atoms but also loads the 3DMOT with a large number of atoms. This creates a favorable starting point for proceeding toward evaporative cooling of the cold atomic mixture to quantum degeneracy.

We have employed two independent and spatially separated 2D$^+$MOTs as the cold atomic beam sources for ^{23}Na and ^{39}K, which

provide cold collimated atomic beams to load the 3DMOT in the UHV chamber through two opposite ports.

A. 2D$^+$MOT

The 2D$^+$MOT is created by two orthogonal retro-reflected elliptical (circular) laser beams in the presence of a two-dimensional quadrupole magnetic field for ^{39}K (^{23}Na) atoms. The elliptical beams chosen are slightly convergent with the $1/e^2$ diameter of the incident beams by 36 mm (24 mm) along the atomic beam direction and by 24 mm (24 mm) normal to the atomic beam axis at the 2D$^+$MOT cloud position for ^{39}K (^{23}Na) atoms. The circularly polarized transverse cooling beams are retro-reflected using right-angled prisms, which preserves the helicity of the beams via two total internal reflections. The degree of convergence has been chosen to accommodate the reflection of the uncoated glass cell surfaces (typically, each surface has 4% reflectance) such that we obtain the same intensities of the incident and the retro-reflected beam at the position of the atomic cloud. The 2D quadrupole magnetic field is realized by two pairs of racetrack coils in an anti-Helmholtz configuration, which creates a line of zero magnetic fields along the center of the magnetic coil configuration. The atoms cooled in the transverse direction are confined around the zero magnetic field line of the 2D quadrupole magnetic field.

The performance of the 2D$^+$MOT is enhanced by integrating a pair of counter-propagating laser beams with a Gaussian width of 12 mm along the atomic beam direction, which forms a longitudinal optical molasses cooling configuration. In this configuration, the optical molasses reduces the longitudinal velocities that allow the atoms to spend more time in the transverse cooling region. This reduces the transverse velocities of the atoms, thereby reducing the divergence of the cold atomic beam. As a result, the atoms go through the differential pumping tube without much loss of atoms, thereby increasing the cold atomic beam flux loading the 3DMOT. The longitudinal cooling beams are referred to as pushing and retarding beams, as shown in Fig. 2. The retarding beam is aligned counter-propagating to the direction of the cold atomic beam. The longitudinal cooling using optical molasses reduces the longitudinal velocity of the cold atomic beam within the capture velocity of the 3DMOT in the UHV chamber, thereby increasing the atoms captured in the 3DMOT. The retarding beam has a dark cylindrical region due to the hole in the mirror overlapping with the pushing beam in the counter-propagating direction, which creates an imbalance in radiation pressure along the shadow region and helps in pushing the cold atomic beam to the UHV chamber through the differential pumping hole. An additional pushing beam with a Gaussian width of 1.15 mm (1.3 mm) for ^{23}Na (^{39}K) was aligned along with the pushing and retarding beams, which pushes the atomic cloud into the 3DMOT chamber.

Two pairs of race-track-shaped magnetic coils in an anti-Helmholtz configuration are placed around the 2D MOT glass cell symmetrically. The transverse magnetic field gradient is 21 G/cm/A (12 G/cm/A) for ^{23}Na (^{39}K).

We use a LabVIEW interfaced PXIe system (NI PXIe 1062Q chassis) containing a digital card (NI 6535) and an analog card (NI 6538) to precisely control the intensity as well as the detuning of the cooling and repumping laser beams through AOMs. In addition, all the trigger lines (required for the camera trigger, RF switches, and IGBT gate trigger for magnetic field switching) are drawn from the digital channels, which have 100 ns time resolution. Acquisition of experimental images is done through a Thorlabs scientific camera (Thorlabs CS2100M) of high quantum efficiency (61% at 600 nm), integrated with LabVIEW.

IV. NUMERICAL SIMULATION

A numerical simulation has been performed to model the characteristics of the 2D$^+$MOT as an atom source to load atoms into the

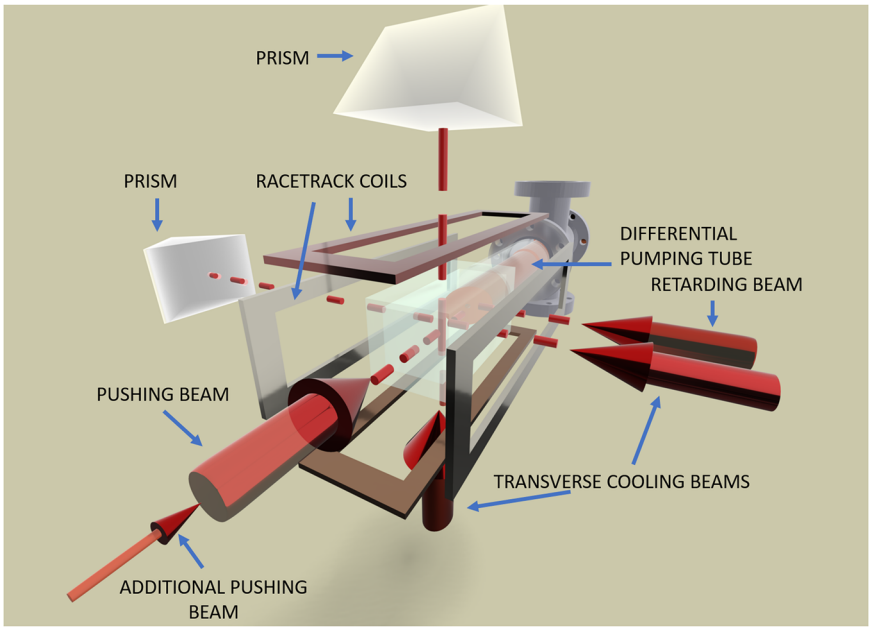

FIG. 2. Schematic diagram of the 2D$^+$MOT. Two transverse cooling beams are retro-reflected using two helicity-preserving right-angled prisms. In addition, a pair of longitudinal cooling beams (pushing and retarding beams) are aligned along the line of the zero magnetic field created due to the configuration of the four race-track-shaped coils. The copper tube with a differential pumping hole connecting the 2D$^+$MOT and the 3DMOT sides is cut at an angle of 45° and mirror-polished to facilitate the passage of the retarding beam. An additional pushing beam is used to direct the cold atomic beam to the 3DMOT chamber through the differential pumping hole.

3DMOT in UHV. In this simulation, the trajectory of each particle captured from background vapor is calculated using their equations of motion. The initial position of the atoms is chosen randomly within the 2D$^+$MOT glass cell excluding the portion containing the copper tube's end that protrudes into the glass cell. The velocities of the atoms are chosen according to the Maxwell–Boltzmann distribution at a certain temperature T (in Kelvin) using the Monte Carlo method. It is assumed that all the particles we will consider for mapping their trajectories have velocities within the capture velocity of that atomic species in the 2D$^+$MOT at that particular temperature. The capture velocity is determined by the temperature of the atoms as well as the intensity, detuning, and size of the cooling beams of the 2D$^+$MOT. After assigning an initial position and velocity to each particle, each of their trajectories is mapped out using the RK4 (Runge–Kutta 4) method in the presence of radiation force due to the cooling laser beams and the magnetic field gradient in the 2D$^+$MOT. While calculating the force, a simplified model of two-level atoms was assumed where the atoms are subjected to the cooling beams, with the frequency red-detuned to the cooling transition. The velocity-dependent force on the atoms is imparted by the four transverse cooling laser beams and a pair of longitudinal cooling beams along the line of the zero magnetic field axis within the 2D$^+$MOT glass cell along the longitudinal Y-direction. The magneto-optical trapping happens only in the transverse directions, determined by the intensity and polarization of the transverse cooling beams as well as the corresponding magnetic-field gradient in the transverse (XZ) directions.

For each axis, the total force on each atom in the 2D$^+$MOT glass cell is contributed from two directions denoted by "+" and the "−" directions of a particular axis. The detuning of the cooling laser beams plays a very important role in determining the force on the atoms. The effective detuning $\delta_\pm$ of the beams is given by

$$\delta_\pm = \delta \pm k \cdot v \mp \mu_{eg} B(r)/\hbar, \tag{1}$$

where δ is the detuning of the laser beam from the atomic resonance. The total magneto-optical force on the atoms is given by $F = F_+ + F_-$, where

$$F_\pm = \pm \frac{\hbar k \Gamma}{2} \frac{s_0}{1 + s_0 + (2\delta_\pm/\Gamma)^2}, \tag{2}$$

where k is the wave vector of the laser beams, $\hbar$ is Planck's constant, Γ is the natural linewidth of the cooling transition, v is the velocity of the atoms, μ_{eg} is the effective magnetic moment for the cooling

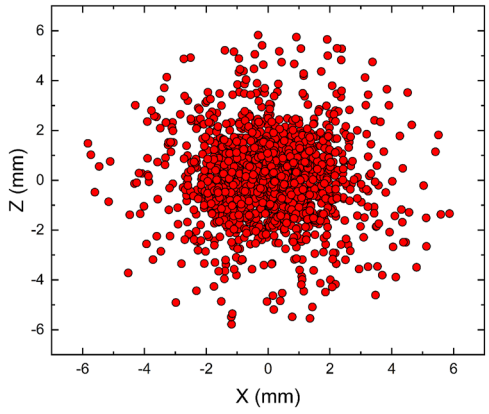

FIG. 3. Final position of the particles on the transverse plane (i.e., XZ plane) at the end of their trajectories at the 3DMOT position.

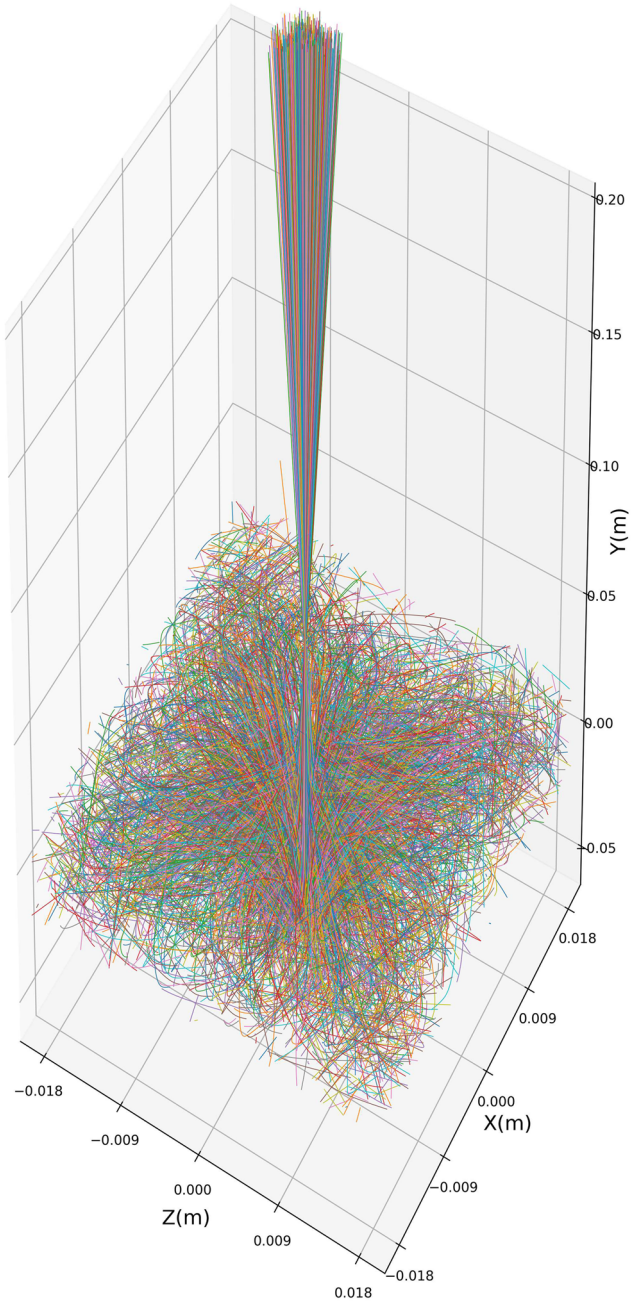

FIG. 4. Trajectory of all the particles coming out of the 2D$^+$MOT glass cell.

transition, $B(r)$ is the magnetic field along the particular axis, and s_0 is the saturation parameter, given by $s_0 = I/I_{sat}$, where I is the intensity of the cooling beams and I_{sat} is the saturation intensity of the atomic transition. Along the longitudinal Z axis, $B(r) = 0$, and for the transverse axes(i.e., X or Y), $B(r) = \sqrt{B_x^2 + B_y^2}$. The "+" and the "–" signs in the force equations are chosen according to the direction in which the force is calculated on the atoms with respect to the center of the 2D$^+$MOT glass cell,

$$\mu_{eg} = (g_e m_{Fe} - g_g m_{Fg})\mu_B, \tag{3}$$

where $g_e m_{Fe}(g_g m_{Fg})$ is calculated for the excited state (ground state) and μ_B is the Bohr magneton. The value of $(g_e m_{Fe} - g_g m_{Fg})$ is obtained as 1 for the D_2 cooling transition of both ^{23}Na and ^{39}K atoms, and hence, $\mu_{eg} = \mu_B$ for both the atomic species.

A. Simulation results

In this section, we present the results obtained from the numerical simulation. The final positions of the particles at the end of their trajectories obtained from the numerical simulation are shown in Fig. 3. The trajectories of all the particles coming out of the 2D$^+$MOT glass cell are shown in Fig. 4. The results of the numerical simulation for the capture rate of the ^{39}K-MOT and the ^{23}Na-MOT as a function of the corresponding 2D$^+$MOT cooling intensity per beam are compared with the corresponding experimental results, as shown in Fig. 7. Since we have performed the simulation by considering typically 10^5 atom trajectories in the cooling volume, whereas the total number of atoms in 2D$^+$MOT cooling volume is governed by the partial pressure, an overall scaling factor is used accordingly. Using the same numerical technique, we have also compared the 2D$^+$MOT flux as a function of the magnetic field gradient with the experimental measurements, as shown in Fig. 10.

TABLE I. Optimized parameters for the 2D$^+$MOTs.

2D$^+$MOT parameters	^{23}Na	^{39}K
$\delta^{2D}_{cooling}$ (Γ)	−1.8	−6.5
$I^{2D}_{cooling}$ per beam (I_S)	7	10
$I^{2D}_{repumping}/I^{2D}_{cooling}$	0.18	0.75
$I^{2D}_{pushing}/I^{2D}_{retarding}$	3.6	8.1
$\partial_x B$, $\partial_z B$ (G/cm)	26	9
$I_{additional-push}$ (I_S)	7.7	5.38
Vapor pressure (mbar)	1.4×10^{-8}	2.2×10^{-7}
3DMOT capture rate (atoms/s)	3.5×10^8	5×10^{10}

V. EXPERIMENTAL RESULTS

For our experiment, the essential parameters that characterize the performance of the two 2D$^+$MOTs are the loading rates into the corresponding 3DMOT for ^{23}Na and ^{39}K atoms. We experimentally studied its dependence on several 2D$^+$MOT parameters, such as the vapor pressure in the 2D$^+$MOT glass cell, the total cooling beam intensities, the 2D$^+$MOT magnetic field gradient, the detuning of the cooling and repumping beams, and the intensity ratios between the repumping and cooling beams, as well as the pushing and retarding beams. The optimized values of these parameters are displayed in Table I. In addition, we have also observed a significant enhancement in the performance of the 2D$^+$MOT for both the atomic species when we use Light Induced Atomic Desorption (LIAD)[56,57] in both the 2D$^+$MOT vacuum manifolds.

We determine the capture rate of atoms in the 3DMOT using fluorescence measurements. We present our typical measurements from the ^{39}K (^{23}Na) 3DMOT using fluorescence images recorded using a CCD camera, as shown in Fig. 5(a) [femtowatt detector in Fig. 5(b)]. The number of atoms in the 3DMOT as a function of the

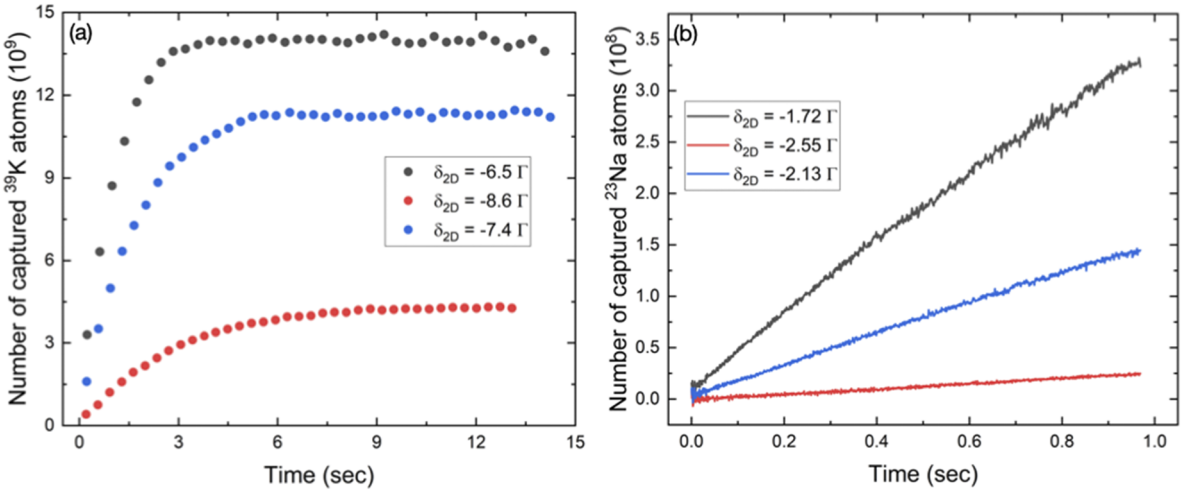

FIG. 5. Number of atoms captured in the (a) ^{39}K-MOT and (b) ^{23}Na-MOT as a function of time for various detunings of the cooling beam of the corresponding 2D$^+$MOT.

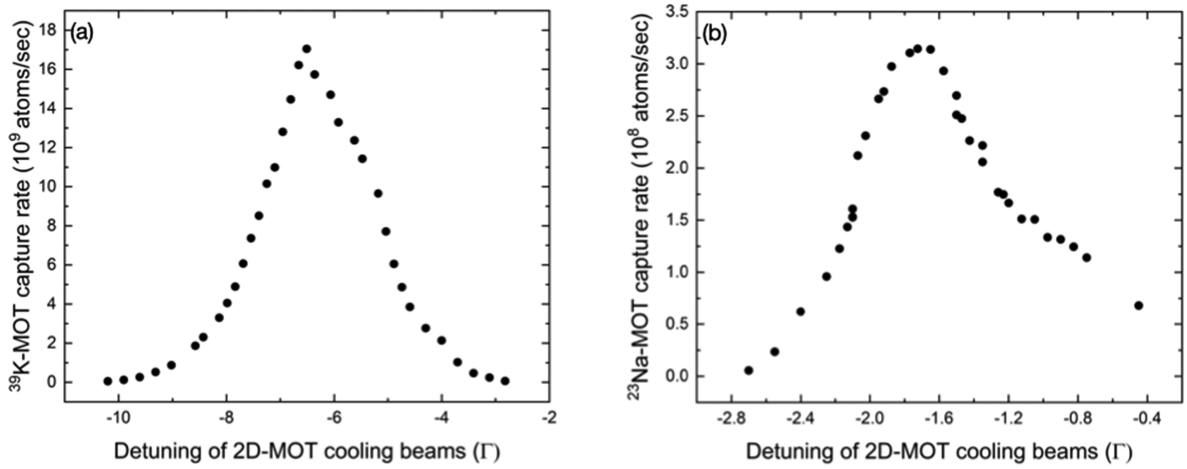

FIG. 6. Capture rate of (a) ^{39}K-MOT and (b) ^{23}Na-MOT as a function of the detuning of the corresponding 2D$^+$MOT cooling beams. The 3DMOT cooling beam detuning was kept fixed at -6.8Γ and -1.4Γ for ^{39}K and ^{23}Na atoms, respectively.

loading time is calculated using the expression for the scattering rate, where the experimental parameters are saturation intensity[58,59] and laser detuning (calibrated using a weak probe beam to determine the exact resonance frequency). The number of atoms captured in the ^{39}K-MOT and ^{23}Na-MOT as a function of time for various detunings of the cooling beam of the corresponding 2D$^+$MOT is shown in Figs. 5(a) and 5(b), respectively. For optimized parameters, we observe a fast loading of 5×10^{10} atoms in 800 ms for ^{39}K atoms. In the case of ^{23}Na atoms, we observe a loading of 5×10^8 atoms in 1.2 s limited only by the two-body collisional loss rate in the bright ^{23}Na 3DMOT.

Figure 6 shows the dependence of the capture rate of the ^{39}K-MOT and the ^{23}Na-MOT on the detuning of the corresponding 2D$^+$MOT cooling beams. The curve has a maximum at detunings of -6.5Γ and -1.8Γ for ^{39}K and ^{23}Na atoms, respectively. The maximum capture rate in the 3DMOT as a function of the detuning of the 2D$^+$MOT cooling beams is the result of two opposing effects: the scattering force of the 2D$^+$MOT beams decreases with increasing detuning, implying a less efficient transverse cooling for higher detuning, whereas the capture velocity increases with higher detuning, which increases the atomic beam flux.[60] The detuning at which the maximum capture rate in the 3DMOT is obtained represents

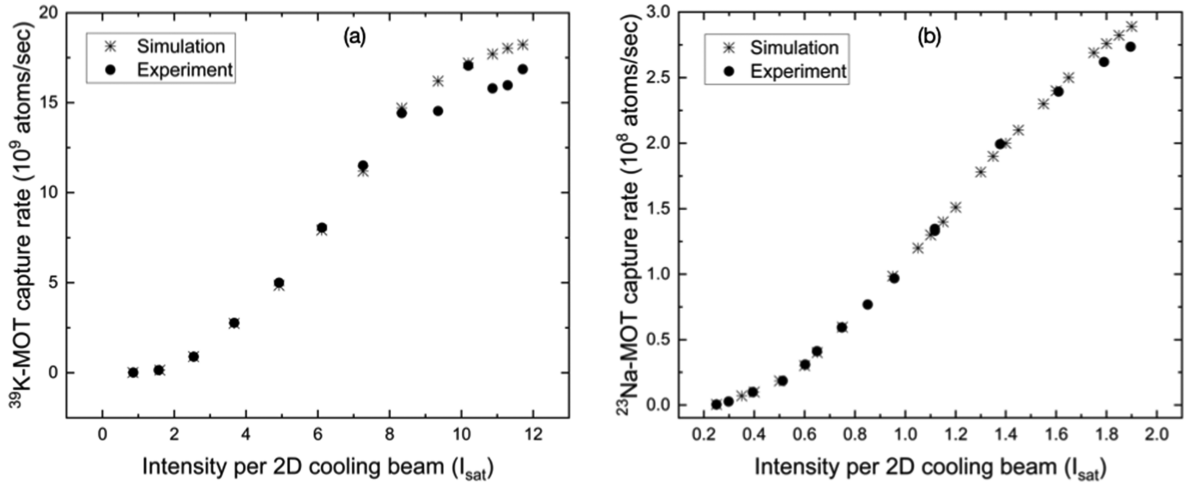

FIG. 7. Experimental measurements and comparison with numerical simulation of the capture rate of (a) ^{39}K-MOT and (b) ^{23}Na-MOT as a function of the corresponding 2D$^+$MOT cooling intensity per beam. The intensity ratios between 2D$^+$MOT repumping and cooling beams were maintained at 0.75 and 0.18 for ^{39}K and ^{23}Na atoms, respectively.

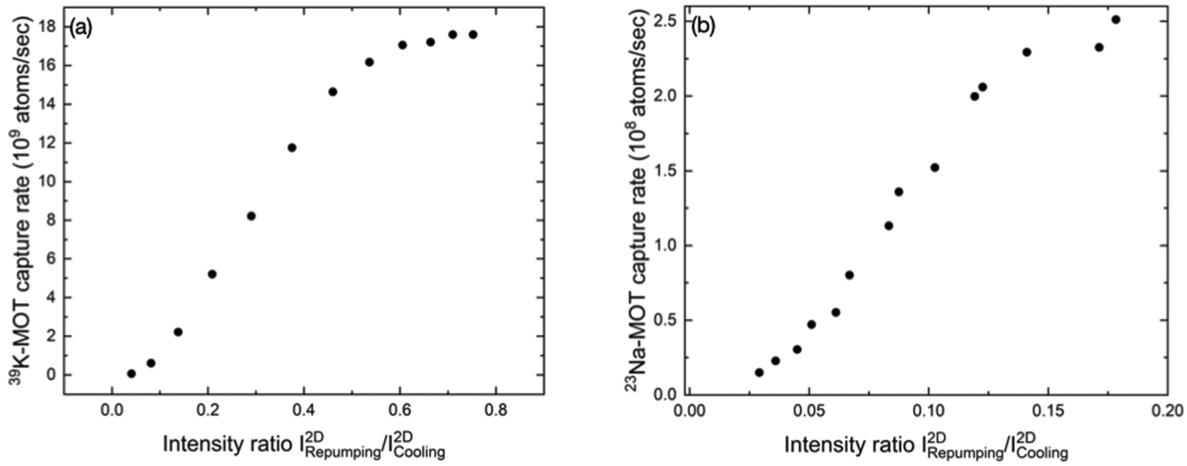

FIG. 8. Capture rate of the (a) ^{39}K-MOT and (b) ^{23}Na-MOT as a function of the intensity ratio between the corresponding $2D^+$ MOT repumping and cooling beams. In the case of ^{39}K atoms, a relatively large repumping to cooling intensity ratio of around 0.75 is required for the optimized operation of the $2D^+$MOT due to the narrow spacing of the excited state hyperfine splitting. On the other hand, the ^{23}Na source works well with a relatively low repumping to cooling intensity ratio of around 0.18.

the detuning for the most efficient transverse cooling of the atoms, which produces a cold atomic beam with high flux and narrow velocity distribution so as to pass through the differential pumping hole with minimum divergence.

An additional factor affecting the behavior of the plot shown in Fig. 6 is that we measure the ^{39}K-MOT and ^{23}Na-MOT capture rate rather than the $2D^+$MOT atomic beam flux. The scattering force of the pushing beam depends on the cooling beam detuning, which is one of the factors that determines the mean velocity of the atomic beam; as a consequence, it has an effect on both the atomic flux[53] and the loading rate of the MOT.[52]

The dependence of the capture rate of the ^{39}K-MOT and the ^{23}Na-MOT on the cooling beam intensity of the corresponding $2D^+$MOT is depicted in Fig. 7. The curve almost linearly increases with the beam power without a clear indication of saturation. The increase is due to two effects: First, the $2D^+$MOT capture velocity increases with laser power due to the power broadening of the atomic spectral lines. Second, the scattering force increases, resulting in steeper transverse confinement, which facilitates the injection of the atoms into the differential pumping tube. The absence of saturation demonstrates that light-induced collisions for the used range of laser powers are negligible. As the rate for light-induced

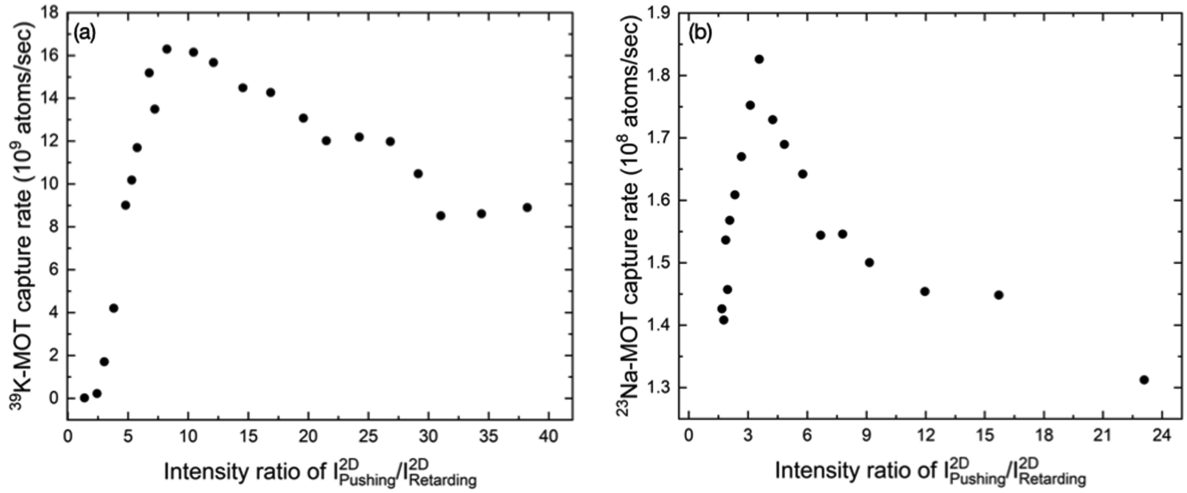

FIG. 9. Capture rate of the (a) ^{39}K-MOT (b) ^{23}Na-MOT as a function of the intensity ratio of the pushing and retarding beams of the corresponding $2D^+$MOT. The optimum value of the intensity ratio is experimentally obtained at 8.1 (3.6) for ^{39}K (^{23}Na) atoms. The data presented in this graph are recorded at a reduced oven temperature whereas we have experimentally checked that the optimum intensity ratio remains the same as a function of partial vapor pressure for both ^{39}K and ^{23}Na atoms.

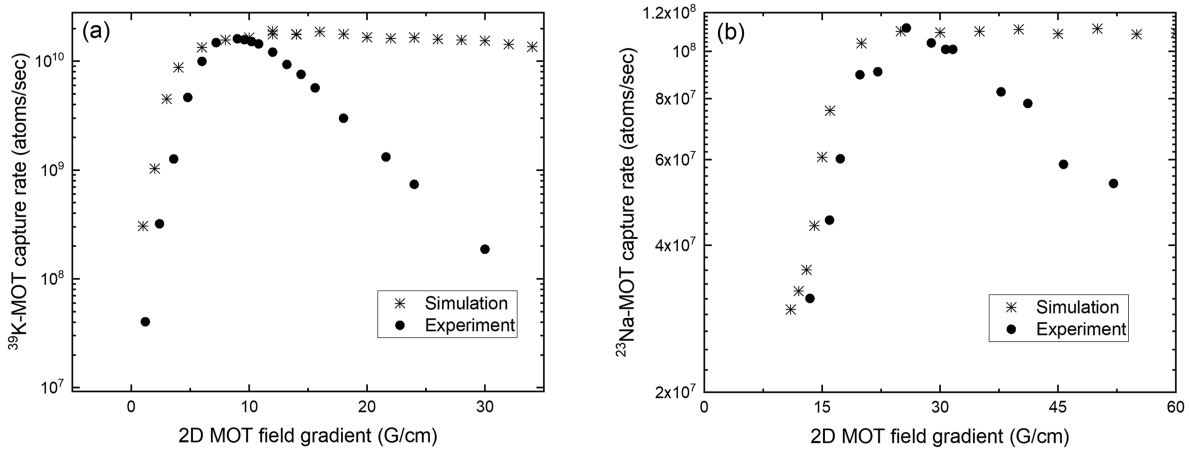

FIG. 10. Experimental results and comparison with the numerical simulation for the capture rate of the (a) ^{39}K-MOT (b) ^{23}Na-MOT as a function of the magnetic field gradient of the corresponding 2D$^+$MOT. At a low magnetic field gradient, the experimental data match well with those of the model developed with simple two-level atom approximation. However, at high field gradients, expectedly, the results deviate especially for potassium atoms where the excited state splitting is less than that of sodium atoms, as elaborated in the text.

collisions depends on the atom number density in the 2D$^+$MOT, the absence of the saturation effect implies that the atomic density in the 2D$^+$MOT is low due to the absence of three-dimensional confinement. This qualitative description given above is supported well using our numerical simulation results, which agree well with the experimental observation, as evident in Fig. 7. The capture rate of atoms in the 3DMOTs is limited by the available laser power in our experiment.

Figure 8 shows the dependence of the capture rate of the ^{39}K-MOT and the ^{23}Na-MOT on the intensity ratio between the cooling and repumping beams of the corresponding 2D$^+$MOT. The graph shows that the ^{39}K-MOT and ^{23}Na-MOT capture rate increases with increasing repumping intensity and that it saturates at high intensities of repumping beams. The dependence of the capture rate on the repumping beam intensity can be attributed to the branching ratio of the transition probabilities for the corresponding atomic transitions in ^{39}K and ^{23}Na atoms. In the case of ^{39}K atoms, the hyperfine splitting of the excited states (dipole allowed from the $|F = 2\rangle$ hyperfine ground state) is small (37.2 MHz), thereby increasing the probability of optical pumping to the lower hyperfine state $|F = 1\rangle$ and removing the atoms from the cooling transition. Hence, a relatively large intensity ratio between the repumping and

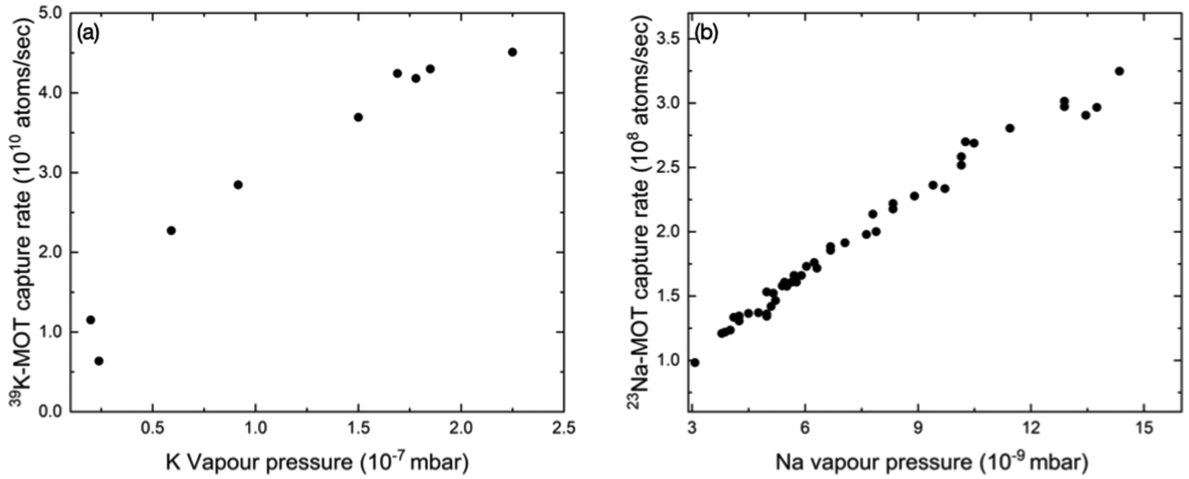

FIG. 11. Capture rate of the (a) ^{39}K-MOT (b) ^{23}Na-MOT as a function of the vapor pressure of ^{39}K and ^{23}Na in their respective 2D$^+$MOTs. We observe a monotonic increase in the 3DMOT capture rates as a function of the 2D$^+$MOT vapor pressure for both species. For ^{39}K, the data indicate a saturation of the capture rate above 2×10^{-7} mbar partial pressure whereas the capture rate for ^{23}Na is only limited by the available partial vapor pressure.

cooling beams is required for the ^{39}K atoms as compared to ^{23}Na atoms where the same excited state hyperfine splitting is relatively large (92.6 MHz).

The dependence of the capture rate of the ^{39}K-MOT and the ^{23}Na-MOT on the intensity ratio between the pushing and retarding beam of the corresponding 2D$^+$MOT is depicted in Fig. 9. The curve has a maximum at $I_{\text{push}}/I_{\text{retard}} = 8.1$ for the ^{39}K-MOT and 3.6 for the ^{23}Na-MOT. The difference observed between the optimized ratio of the pushing and retarding beams for ^{39}K and ^{23}Na 2D$^+$MOTs can be attributed to the following argument. The ^{23}Na atoms tend to diffuse out of the cooling volume due to lower mass and larger scattering rates than the ^{39}K atoms. Therefore, we need to also efficiently cool the ^{23}Na atoms in the longitudinal direction so that they spend a longer duration in the transverse cooling region. This is achieved by a smaller $I_{\text{push}}/I_{\text{retard}}$ ratio than the ^{39}K atoms.

The dependence of the capture rate of the ^{39}K-MOT and the ^{23}Na-MOT on the magnetic field gradient of the corresponding 2D$^+$MOT is shown in Fig. 10. The curves show a maximum capture rate of the 3DMOT at the 2D$^+$MOT magnetic field gradient of 8 and 25 G/cm for ^{39}K and ^{23}Na atoms, respectively, depicting the optimized 2D$^+$MOT magnetic field gradient for efficient magneto-optical confinement in the transverse direction so as to pass through the differential pumping hole with minimum loss of atoms. We have compared this observation with the numerical simulation results and found that at low magnetic field gradients, the agreement is good for both species. However, at a high field, the simple two-level model is no longer a valid approximation because the excited state manifold (spacing between $|F' = 1\rangle$ and $|F' = 3\rangle$ states) in the case of potassium is pretty small (~31 MHz) while it is around ~93 MHz for sodium. Therefore, the force on an atom away from the 2D-MOT center axis is significantly high for the high gradient case compared to what is calculated using a simple two-level model. This effect, in turn, increases the atomic beam divergence, limiting the capture rate into the 3DMOT. Expectedly, this effect is more serious in the case of potassium than sodium, as is evident from Fig. 10.

TABLE II. Optimized parameters for the 3DMOT.

3DMOT parameters	^{23}Na	^{39}K
$\delta^{3D}_{cooling}$ (Γ)	−1.4	−6.8
Total $I^{3D}_{cooling}$ (I_S)	10	22.7
3DMOT field gradient (G/cm)	17.6	18.5
$I^{3D}_{repumping}/I^{3D}_{cooling}$	0.225	0.75
Total number of atoms	5.8×10^8	3×10^{10}

Figure 11 shows the dependence of the ^{39}K-MOT and ^{23}Na-MOT capture rate on the vapor pressure of ^{39}K as well as ^{23}Na atoms in the 2D$^+$MOT cell. The vapor pressure was measured by recording the absorption profile of a low-intensity probe, fitting it to Beer's law and applying the ideal gas equation. For the fit, the isotopic abundance in the cell needs to be taken into account as small hyperfine splittings and isotopic shifts of the potassium atoms lead to a single Doppler absorption profile induced by different transitions. As evident from the plots in Fig. 11, the capture rate in the 3DMOT increases linearly with vapor pressure in the 2D$^+$MOT glass cell for both ^{39}K and ^{23}Na atoms for low partial vapor pressures. We observe an indication of saturation in the capture rate for the ^{39}K source at around 2×10^{-7} mbar vapor pressure. The capture rate for the ^{23}Na 3DMOT is only limited by the available partial vapor pressure of ^{23}Na atoms in the 2D$^+$MOT glass cell. The ^{23}Na partial vapor pressure was not measured using the weak probe absorption technique; rather it was inferred from the temperature of the air around the glass cell.

The optimized experimental parameters for the ^{39}K and ^{23}Na 2D$^+$MOTs are summarized in Table I, and the optimized parameters for the ^{39}K and ^{23}Na 3DMOTs are summarized in Table II.

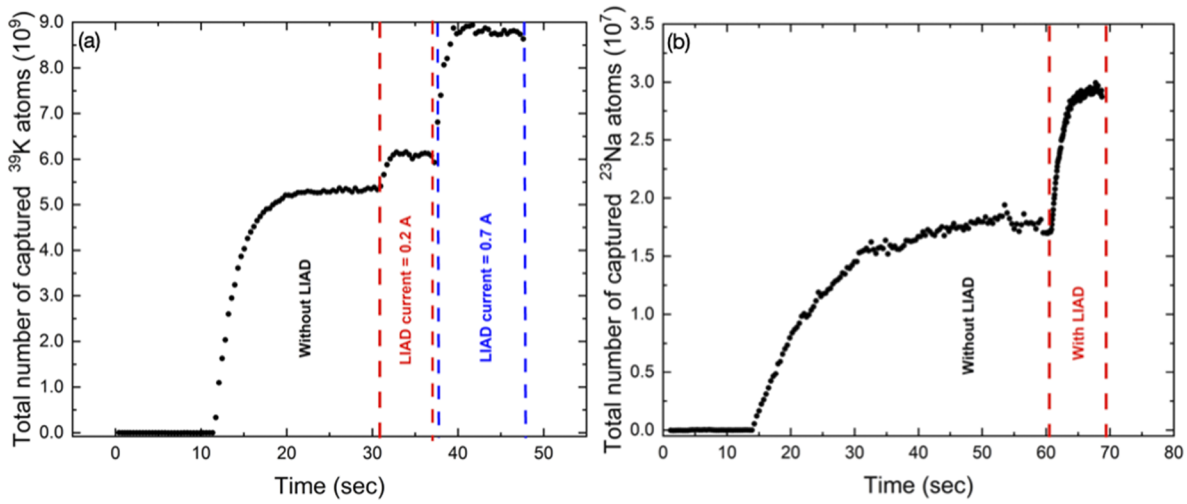

FIG. 12. Total number of atoms captured in the (a) ^{39}K-MOT (b) ^{23}Na-MOT as a function of time, demonstrating the effect of switching on the LIAD (light-induced atomic desorption) for the corresponding 2D$^+$MOT.

In order to vary the vapor pressure in the $2D^+$MOT side for ^{39}K atoms, the oven temperature was varied between 50 and 130 °C. The metal parts near the $2D^+$MOT glass cell were kept mildly heated to 40 °C so as to prevent coating of ^{39}K atoms there and to facilitate ^{39}K atomic vapor coming into the glass cell. In the case of the ^{23}Na $2D^+$MOT, the oven was heated to 300 °C, and the metal parts near the glass cell were heated to 100 °C. The region around the ^{23}Na $2D^+$MOT glass cell was kept heat-insulated using a heat-insulation blanket and two layers of aluminum foil while keeping sufficient openings for the cooling laser beams. Heating rods were inserted inside the insulated region to keep the air temperature around the $2D^+$MOT glass cell between 60 and 75 °C. In the case of Na, this special arrangement is done (in contrast to ^{39}K) because ^{23}Na atoms have a particular tendency to stick to glass surfaces and the melting point of ^{23}Na is also relatively high (98 °C). We have avoided heating the glass cell to a higher temperature so as to prevent degrading the vacuum at the $2D^+$MOT side.

The total number of atoms captured in the ^{39}K-MOT and ^{23}Na-MOT as a function of time demonstrating the effect of switching on LIAD (light-induced atomic desorption) for the corresponding $2D^+$MOT is shown in Fig. 12. In our experiment, LIAD plays a significant role in increasing the vapor pressure of ^{39}K and ^{23}Na atoms in their respective $2D^+$MOT glass cells by increasing the atomic beam flux and thereby the capture rate of atoms in the corresponding 3DMOT. We use commercially available high-power UV Light-Emitting Diodes (LEDs) (center wavelength of 395 nm) (Thorlabs M395L5) for the ^{39}K side and a 100 low-power UV LED array for the ^{23}Na side. Both ^{39}K and ^{23}Na atoms are efficiently desorbed from the glass surface upon shining the UV light, thereby increasing the partial pressure of the atoms without affecting the overall vacuum in the $2D^+$MOT glass cells. This results in a significant increase in the $2D^+$MOT flux as well as the 3DMOT capture rate, as shown in Fig. 12. This is particularly useful because apart from the improved performance of the cold atom sources, the UV light also prevents the glass surface from being coated by ^{39}K and ^{23}Na atoms.

VI. LIGHT-ASSISTED INTERSPECIES COLD COLLISIONS

Finally, we report on the effect of cold collisions between ^{23}Na and ^{39}K atoms while they are simultaneously captured in the 3DMOT. The effects are considerable and may cause significant atom loss from the trap, as evident from the typical experimental data shown in the inset of Fig. 13, where we monitored only the number of ^{23}Na trapped atoms while loading the ^{39}K 3DMOT, which overlaps with the ^{23}Na 3DMOT in space. From a series of such data recorded with different ^{39}K loading rates, we experimentally found an interspecies loss-coefficient (β_{NaK}). We present the results as a survival probability of one species (reported for ^{23}Na) in the presence of the other species by calculating the total trap loss in the asymptotic limit (Fig. 13). In this context, the survival probability is defined as the fraction of atoms remaining after the interspecies light assisted collision is turned on.

It is worth noting that we observe as much as nearly 50% loss of ^{23}Na atoms due to interspecies light assisted cold collisions. As the ^{39}K numbers are increased in the trap by increasing the ^{39}K $2D^+$MOT flux, the interspecies collisions result in further loss of ^{23}Na atoms, which saturates above a mixture ratio (the ratio of the

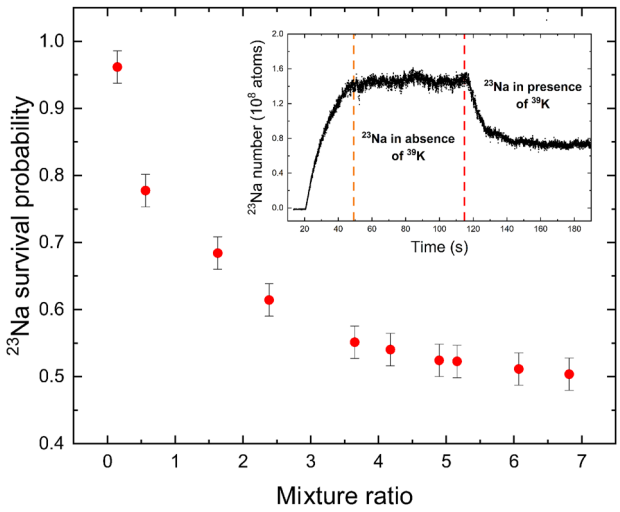

FIG. 13. Survival probability of ^{23}Na atoms as a function of the "mixture ratio" (ratio between the number of ^{39}K and ^{23}Na atoms). Inset: Typical data of the ^{23}Na atom number in the 3DMOT in the absence and presence of ^{39}K 3DMOT loading.

number of ^{39}K atoms to the ^{23}Na atoms in the trap) of 5. In this high mixture ratio, ^{39}K can be considered a bath in which ^{23}Na atoms move as "impurities". As the bath size is increased, we reach a constant density limit for the ^{39}K cloud, and the interspecies collision also reaches a steady state value. For typical dual species overlapping 3DMOTs of ^{23}Na and ^{39}K, we find the interspecies loss co-efficient, $\beta_{NaK} = 2 \times 10^{-12}$ cm^3/sec (using the semi-classical approach described in Ref. 61). In comparison, the intra-species light-assisted collision rate for ^{23}Na–^{23}Na is $\beta_{NaNa} = 2.1 \times 10^{-11}$ cm^3/sec, and that for ^{39}K–^{39}K is $\beta_{KK} = 3 \times 10^{-11}$ cm^3/sec. These measurements are performed using the typical single species loading curves in the 3DMOT using a similar measurement technique described in Ref. 62.

In order to verify the above-mentioned argument physically, we varied the interspecies loss-coefficient (β_{NaK}) by varying the excited state population of the bath atoms (^{39}K). Experimentally, this is performed by controlling the repump laser power in the 3DMOT, which regulates the population of the ^{39}K atoms in the $|F = 2\rangle$ state. The resulting data are presented in Fig. 14. The observation indicates that as the excited state population is increased, the interspecies collision rate also increases, resulting in further decrease in the number of minority species (^{23}Na) atoms. Interestingly, beyond a certain excited state fraction of around 1.75% in ^{39}K atoms, the survival probability of the ^{23}Na atoms actually increases again. This is because at such high ^{39}K excited state population, ^{39}K–^{39}K collisions (governed by the C_3/R^3 potential) dominate the ^{23}Na–^{39}K collisions (which are governed through C_6/R^6 potential).[63] Here, R is the inter-atomic separation, and C_3 and C_6 are the resonant and off-resonant dipole–dipole interaction coefficients, respectively. This effect results in the decrease in the density of the majority species (^{39}K) and hence the interspecies collision rates. This observation suggests that the interspecies collision can be tuned and significantly reduced by controlling the excited state population of

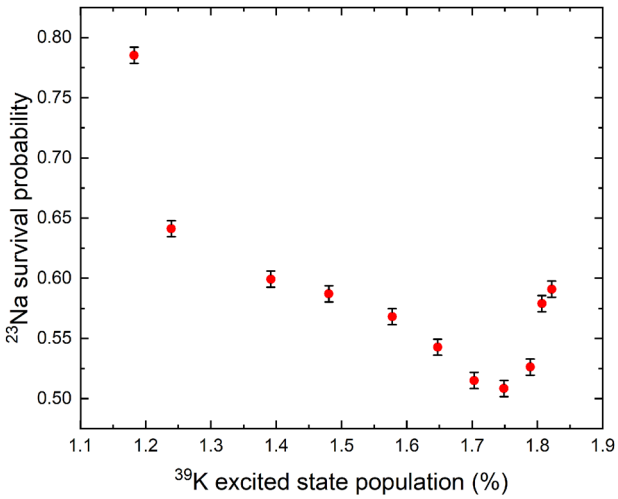

FIG. 14. Survival probability of ^{23}Na atoms as a function of the excited state population of the ^{39}K atoms.

the bath. This way, we could vary β_{NaK} in a range between 1.7 and 3.3×10^{-12} cm^3/sec.

VII. CONCLUSION AND OUTLOOK

We report the design, implementation, and characterization of two 2D$^+$MOT sources of a cold atomic beam for ^{39}K and ^{23}Na atoms. We characterize the performance of the two 2D$^+$MOTs via measurements of the capture rate of atoms in the corresponding 3DMOT. We studied both experimentally and using a comprehensive numerical simulation the dependence of the capture rate of cold atoms in the 3DMOT on the various 2D$^+$MOT parameters for both ^{39}K and ^{23}Na atoms. In this way, we obtain the optimized values of these parameters to ensure the best performance of the cold atomic beam sources. Joint performance of the overlapping ^{23}Na and ^{39}K MOTs has been studied, and interspecies light-assisted collisional processes are reported along with the interspecies collision rates.

The cold atomic mixture will be cooled further via sub-Doppler cooling and loaded into a magnetic trap. Subsequently, the atoms would be transported to a "science cell" located at a distance of about 51 cm from the MOT center using a magnetic transport and thereafter loaded into a QUIC magnetic trap for RF evaporative cooling to reach simultaneous quantum degeneracy of ^{23}Na and ^{39}K atoms. The quantum degenerate mixture would thereafter be transferred into optical traps and optical lattices[64] for further experiments on quantum simulation of interacting many-body systems.[2] The response function of the cold atoms[65] can be studied in the presence of inter-species interaction, exploring a rich parameter space for the measurements. The spin-exchange interaction between hetero-nuclear cold atomic mixtures can be studied using Faraday rotation fluctuation measurements.[66] Our compact and versatile setup for realizing cold atomic beam sources of ^{39}K and ^{23}Na atoms will be useful for experiments on a quantum degenerate mixture of ^{39}K and ^{23}Na atoms, and it can be utilized for a variety of quantum technology experiments, such as quantum metrology,[67] quantum simulation,[68] and quantum sensing.[69]

ACKNOWLEDGMENTS

This work was partially supported by the Ministry of Electronics and Information Technology (MeitY), Government of India, through the Center for Excellence in Quantum Technology, under Grant No. 4(7)/2020-ITEA. S.R. acknowledges funding from the Department of Science and Technology, India, via WOS-A project Grant No. SR/WOS-A/PM-59/2019. We acknowledge M. S. Meena, Md. Ibrahim, S. Barui, S. Sujatha, S. Bhar, B. B. Boruah, S. Bagchi, the RRI mechanical workshop, and the RRI HPC facility for assistance with the experiments and for the instruments.

AUTHOR DECLARATIONS

Conflict of Interest

The authors have no conflicts to disclose.

Author Contributions

Sagar Sutradhar: Conceptualization (equal); Data curation (equal); Formal analysis (equal); Investigation (equal); Methodology (equal); Writing – original draft (equal); Writing – review & editing (equal). **Anirban Misra**: Data curation (equal); Formal analysis (equal); Investigation (equal); Methodology (equal); Writing – original draft (equal); Writing – review & editing (equal). **Gourab Pal**: Data curation (lead); Formal analysis (equal); Investigation (equal); Methodology (equal); Writing – original draft (equal); Writing – review & editing (equal). **Sayari Majumder**: Data curation (lead); Formal analysis (equal); Investigation (equal); Methodology (equal); Writing – original draft (equal); Writing – review & editing (equal). **Sanjukta Roy**: Conceptualization (equal); Data curation (equal); Formal analysis (supporting); Funding acquisition (equal); Investigation (equal); Methodology (equal); Project administration (equal); Writing – original draft (lead); Writing – review & editing (lead). **Saptarishi Chaudhuri**: Conceptualization (equal); Data curation (equal); Formal analysis (equal); Funding acquisition (equal); Investigation (equal); Methodology (equal); Project administration (equal); Supervision (equal); Writing – original draft (equal); Writing – review & editing (equal).

DATA AVAILABILITY

The data that support the findings of this study are available from the corresponding author upon reasonable request.

REFERENCES

[1] I. Bloch, J. Dalibard, and W. Zwerger, "Many-body physics with ultracold gases," Rev. Mod. Phys. **80**, 885–964 (2008).
[2] I. Bloch, J. Dalibard, and S. Nascimbène, "Quantum simulations with ultracold quantum gases," Nat. Phys. **8**, 267–276 (2012).
[3] C. Gross and I. Bloch, "Quantum simulations with ultracold atoms in optical lattices," Science **357**, 995–1001 (2017).
[4] F. Schäfer, T. Fukuhara, S. Sugawa, Y. Takasu, and Y. Takahashi, "Tools for quantum simulation with ultracold atoms in optical lattices," Nat. Rev. Phys. **2**, 411–425 (2020).

[5]J. H. Denschlag, J. E. Simsarian, H. Häffner, C. McKenzie, A. Browaeys, D. Cho, K. Helmerson, S. L. Rolston, and W. D. Phillips, "A Bose–Einstein condensate in an optical lattice," J. Phys. B: At., Mol. Opt. Phys. **35**, 3095–3110 (2002).
[6]J. Ye, S. Blatt, M. M. Boyd, S. M. Foreman, E. R. Hudson, T. Ido, B. Lev, A. D. Ludlow, B. C. Sawyer, B. Stuhl, and T. Zelinsky, "Precision measurement and frequency metrology with ultracold atoms measurement based on ultracold atoms and cold molecules," Int. J. Mod. Phys. D **16**, 2481–2494 (2007).
[7]X. Zhang and J. Ye, "Precision measurement and frequency metrology with ultracold atoms," Natl. Sci. Rev. **3**, 189 (2016).
[8]C. J. Myatt, E. A. Burt, R. W. Ghrist, E. A. Cornell, and C. E. Wieman, "Production of two overlapping Bose–Einstein condensates by sympathetic cooling," Phys. Rev. Lett. **78**, 586–589 (1997).
[9]D. S. Hall, M. R. Matthews, J. R. Ensher, C. E. Wieman, and E. A. Cornell, "Dynamics of component separation in a binary mixture of Bose–Einstein condensates," Phys. Rev. Lett. **81**, 1539–1542 (1998).
[10]J. Stenger, S. Inouye, D. M. Stamper-Kurn, H.-J. Miesner, A. P. Chikkatur, and W. Ketterle, "Spin domains in ground-state Bose–Einstein condensates," Nature **396**, 345–348 (1998).
[11]G. Modugno, G. Ferrari, G. Roati, R. J. Brecha, A. Simoni, and M. Inguscio, "Bose–Einstein condensation of potassium atoms by sympathetic cooling," Science **294**, 1320–1322 (2001).
[12]Z. Hadzibabic, C. A. Stan, K. Dieckmann, S. Gupta, M. W. Zwierlein, A. Görlitz, and W. Ketterle, "Two-species mixture of quantum degenerate Bose and Fermi gases," Phys. Rev. Lett. **88**, 160401 (2002).
[13]G. Modugno, M. Modugno, F. Riboli, G. Roati, and M. Inguscio, "Two atomic species superfluid," Phys. Rev. Lett. **89**, 190404 (2002).
[14]C. A. Regal, M. Greiner, and D. S. Jin, "Observation of resonance condensation of Sonic atom pairs," Phys. Rev. Lett. **92**, 040403 (2004).
[15]C. Silber, S. Günther, C. Marzok, B. Deh, P. W. Courteille, and C. Zimmermann, "Quantum-degenerate mixture of fermionic lithium and bosonic rubidium gases," Phys. Rev. Lett. **95**, 170408 (2005).
[16]K. Günter, T. Stöferle, H. Moritz, M. Köhl, and T. Esslinger, "Bose-Fermi mixtures in a three-dimensional optical lattice," Phys. Rev. Lett. **96**, 180402 (2006).
[17]S. B. Papp, J. M. Pino, and C. E. Wieman, "Tunable miscibility in a dual-species Bose–Einstein condensate," Phys. Rev. Lett. **101**, 040402 (2008).
[18]S. Ospelkaus, C. Ospelkaus, O. Wille, M. Succo, P. Ernst, K. Sengstock, and K. Bongs, "Localization of bosonic atoms by fermionic impurities in a three-dimensional optical lattice," Phys. Rev. Lett. **96**, 180403 (2006).
[19]J. Catani, L. De Sarlo, G. Barontini, F. Minardi, and M. Inguscio, "Degenerate Bose-Bose mixture in a three-dimensional optical lattice," Phys. Rev. A **77**, 011603 (2008).
[20]M. Taglieber, A. C. Voigt, T. Aoki, T. W. Hänsch, and K. Dieckmann, "Quantum degenerate two-species Fermi-Fermi mixture coexisting with a Bose–Einstein condensate," Phys. Rev. Lett. **100**, 010401 (2008).
[21]D. J. McCarron, H. W. Cho, D. L. Jenkin, M. P. Köppinger, and S. L. Cornish, "Dual-species Bose–Einstein condensate of ^{87}Rb and ^{133}Cs," Phys. Rev. A **84**, 011603(R) (2011).
[22]B. Pasquiou, A. Bayerle, S. M. Tzanova, S. Stellmer, J. Szczepkowski, M. Parigger, R. Grimm, and F. Schreck, "Quantum degenerate mixtures of strontium and rubidium atoms," Phys. Rev. A **88**, 023601 (2013).
[23]I. Ferrier-Barbut, M. Delehaye, S. Laurent, A. T. Grier, M. Pierce, B. S. Rem, F. Chevy, and C. Salomon, "A mixture of Bose and Fermi superfluids," Science **345**, 1035–1038 (2014).
[24]L. Wacker, N. B. Jørgensen, D. Birkmose, R. Horchani, W. Ertmer, C. Klempt, N. Winter, J. Sherson, and J. J. Arlt, "Tunable dual-species Bose–Einstein condensates of ^{39}K and ^{87}Rb," Phys. Rev. A **92**, 053602 (2015).
[25]C. Ravensbergen, V. Corre, E. Soave, M. Kreyer, E. Kirilov, and R. Grimm, "Production of a degenerate Fermi-Fermi mixture of dysprosium and potassium atoms," Phys. Rev. A **98**, 063624 (2018).
[26]P. C. M. Castilho, E. Pedrozo-Peñafiel, E. M. Gutierrez, P. L. Mazo, G. Roati, K. M. Farias, and V. S. Bagnato, "A compact experimental machine for studying tunable Bose–Bose superfluid mixtures," Laser Phys. Lett. **16**, 035501 (2019).
[27]A. P. Chikkatur, A. Görlitz, D. M. Stamper-Kurn, S. Inouye, S. Gupta, and W. Ketterle, "Suppression and enhancement of impurity scattering in a Bose–Einstein condensate," Phys. Rev. Lett. **85**, 483–486 (2000).
[28]Gal Ness, Constantine Shkedrov, Yanay Florshaim, Oriana K. Diessel, Jonas von Milczewski, Richard Schmidt, and Yoav Sagi, "Observation of a Smooth Polaron-Molecule Transition in a Degenerate Fermi Gas," Phys. Rev. X **10**(4), 041019 (2020).
[29]M. Bruderer, A. Klein, S. Clark, and D. Jaksch, "Transport of strong-coupling polarons in optical lattices," New J. Phys. **10**, 033015 (2007).
[30]D. S. Petrov, "Quantum mechanical stabilization of a collapsing Bose–Bose mixture," Phys. Rev. Lett. **115**, 155302 (2015).
[31]C. R. Cabrera, L. Tanzi, J. Sanz, B. Naylor, P. Thomas, P. Cheiney, and L. Tarruell, "Quantum liquid droplets in a mixture of Bose–Einstein condensates," Science **359**, 301–304 (2018).
[32]G. Semeghini, G. Ferioli, L. Masi, C. Mazzinghi, L. Wolswijk, F. Minardi, M. Modugno, G. Modugno, M. Inguscio, and M. Fattori, "Self-bound quantum droplets of atomic mixtures in free space," Phys. Rev. Lett. **120**, 235301 (2018).
[33]C. D'Errico, A. Burchianti, M. Prevedelli, L. Salasnich, F. Ancilotto, M. Modugno, F. Minardi, and C. Fort, "Observation of quantum droplets in a heteronuclear bosonic mixture," Phys. Rev. Research **1**, 033155 (2019).
[34]P. S. Żuchowski and J. M. Hutson, "Reactions of ultracold alkali-metal dimers," Phys. Rev. A **81**, 060703(R) (2010).
[35]K. K. Voges, P. Gersema, M. Meyer zum Alten Borgloh, T. A. Schulze, T. Hartmann, A. Zenesini, and S. Ospelkaus, "Ultracold gas of bosonic ^{23}Na^{39}K ground-state molecules," Phys. Rev. Lett. **125**, 083401 (2020).
[36]J. Park, S. Will, and M. Zwierlein, "Ultracold dipolar gas of fermionic ^{23}Na^{40}K molecules in their absolute ground state," Phys. Rev. Lett. **114**, 205302 (2015).
[37]S. Ospelkaus, K.-K. Ni, D. Wang, M. H. G. de Miranda, B. Neyenhuis, G. Quéméner, P. S. Julienne, J. L. Bohn, D. S. Jin, and J. Ye, "Quantum-state controlled chemical reactions of ultracold potassium-rubidium molecules," Science **327**, 853–857 (2010).
[38]L. De Marco, G. Valtolina, K. Matsuda, W. G. Tobias, J. P. Covey, and J. Ye, "A degenerate Fermi gas of polar molecules," Science **363**, 853–856 (2019).
[39]T. Takekoshi, L. Reichsöllner, A. Schindewolf, J. M. Hutson, C. R. Le Sueur, O. Dulieu, F. Ferlaino, R. Grimm, and H.-C. Nägerl, "Ultracold dense samples of dipolar RbCs molecules in the rovibrational and hyperfine ground state," Phys. Rev. Lett. **113**, 205301 (2014).
[40]B. Damski, L. Santos, E. Tiemann, M. Lewenstein, S. Kotochigova, P. Julienne, and P. Zoller, "Creation of a dipolar superfluid in optical lattices," Phys. Rev. Lett. **90**, 110401 (2003).
[41]T. Lahaye, C. Menotti, L. Santos, M. Lewenstein, and T. Pfau, "The physics of dipolar bosonic quantum gases," Rep. Prog. Phys. **72**, 126401 (2009).
[42]A. Schindewolf, R. Bause, X.-Y. Chen, M. Duda, T. Karman, I. Bloch, and X.-Y. Luo, "Evaporation of microwave-shielded polar molecules to quantum degeneracy," Nature **607**, 677–681 (2022).
[43]S. A. Will, J. W. Park, Z. Z. Yan, H. Loh, and M. W. Zwierlein, "Coherent microwave control of ultracold ^{23}Na^{40}K molecules," Phys. Rev. Lett. **116**, 225306 (2016).
[44]M. Baranov, "Theoretical progress in many-body physics with ultracold dipolar gases," Phys. Rep. **464**, 71–111 (2008).
[45]W. D. Phillips and H. Metcalf, "Laser deceleration of an atomic beam," Phys. Rev. Lett. **48**, 596–599 (1982).
[46]Z. T. Lu, K. L. Corwin, M. J. Renn, M. H. Anderson, E. A. Cornell, and C. E. Wieman, "Low-velocity intense source of atoms from a magneto-optical trap," Phys. Rev. Lett. **77**, 3331–3334 (1996).
[47]J. Schoser, A. Batär, R. Löw, V. Schweikhard, A. Grabowski, Y. B. Ovchinnikov, and T. Pfau, "Intense source of cold Rb atoms from a pure two-dimensional magneto-optical trap," Phys. Rev. A **66**, 023410 (2002).
[48]S. Chaudhuri, S. Roy, and C. S. Unnikrishnan, "Realization of an intense cold Rb atomic beam based on a two-dimensional magneto-optical trap: Experiments and comparison with simulations," Phys. Rev. A **74**, 023406 (2006).
[49]K. Dieckmann, R. J. C. Spreeuw, M. Weidemüller, and J. T. M. Walraven, "Two-dimensional magneto-optical trap as a source of slow atoms," Phys. Rev. A **58**, 3891–3895 (1998).
[50]S. Ravenhall, B. Yuen, and C. Foot, "High-flux, adjustable, compact cold-atom source," Opt. Express **29**, 21143–21159 (2021).
[51]K. M. R. van der Stam, E. D. van Ooijen, R. Meppelink, J. M. Vogels, and P. van der Straten, "Large atom number Bose–Einstein condensate of sodium," Rev. Sci. Instrum. **78**, 013102 (2007).

[52]E. Pedrozo-Peñafiel, F. Vivanco, P. Castilho, R. R. Paiva, K. M. Farias, and V. S. Bagnato, "Direct comparison between a two-dimensional magneto-optical trap and a Zeeman slower as sources of cold sodium atoms," Laser Phys. Lett. **13**, 065501 (2016).
[53]J. Catani, P. Maioli, L. De Sarlo, F. Minardi, and M. Inguscio, "Intense slow beams of bosonic potassium isotopes," Phys. Rev. A **73**, 033415 (2006).
[54]M. Gröbner, P. Weinmann, F. Meinert, K. Lauber, E. Kirilov, and H.-C. Nägerl, "A new quantum gas apparatus for ultracold mixtures of K and Cs and KCs ground-state molecules," J. Mod. Opt. **63**, 1829–1839 (2016).
[55]G. Lamporesi, S. Donadello, S. Serafini, and G. Ferrari, "Compact high-flux source of cold sodium atoms," Rev. Sci. Instrum. **84**, 063102 (2013).
[56]G. Telles, T. Ishikawa, M. Gibbs, and C. Raman, "Light-induced atomic desorption for loading a sodium magneto-optical trap," Phys. Rev. A **81**, 032710 (2010).
[57]L. Torralbo-Campo, G. D. Bruce, G. Smirne, and D. Cassettari, "Light-induced atomic desorption in a compact system for ultracold atoms," Sci. Rep. **5**, 14729 (2015).
[58]J. M. Kwolek, D. S. Goodman, S. A. Entner, J. E. Wells, F. A. Narducci, and W. W. Smith, "Model-independent measurements of the sodium magneto-optical trap's excited-state population," Phys. Rev. A **97**, 053420 (2018).
[59]R. S. Williamson and T. Walker, "Magneto-optical trapping and ultracold collisions of potassium atoms," J. Opt. Soc. Am. B **12**, 1393–1397 (1995).
[60]H. Metcalf, P. Van der Straten, J. Birman, J. Lynn, and H. Stanley, *Laser Cooling and Trapping*, *Graduate Texts in Contemporary Physics* (Springer, 1999).
[61]G. D. Telles, W. Garcia, L. G. Marcassa, V. S. Bagnato, D. Ciampini, M. Fazzi, J. H. Müller, D. Wilkowski, and E. Arimondo, "Trap loss in a two-species Rb-Cs magneto-optical trap," Phys. Rev. A **63**, 033406 (2001).
[62]T. P. Dinneen, K. R. Vogel, E. Arimondo, J. L. Hall, and A. Gallagher, "Cold collisions of Sr^*–Sr in a magneto-optical trap," Phys. Rev. A **59**, 1216–1222 (1999).
[63]M. S. Santos, P. Nussenzveig, A. Antunes, P. S. P. Cardona, and V. S. Bagnato, "Hyperfine-changing collision measurements in trap loss for mixed species in a magneto-optical trap," Phys. Rev. A **60**, 3892–3895 (1999).
[64]S. Chaudhuri, S. Roy, and C. S. Unnikrishnan, "Bose–Einstein condensation in optical traps and in a 1D optical lattice," Curr. Sci. **95**(8), 1026–1034 (2008).
[65]S. Bhar, M. Swar, U. Satpathi, S. Sinha, R. Sorkin, S. Chaudhuri, and S. Roy, "Measurements and analysis of response function of cold atoms in optical molasses," Opt. Continuum **1**, 171–188 (2022).
[66]M. Swar, D. Roy, S. Bhar, S. Roy, and S. Chaudhuri, "Detection of spin coherence in cold atoms via faraday rotation fluctuations," Phys. Rev. Res. **3**, 043171 (2021).
[67]M. Oszmaniec, R. Augusiak, C. Gogolin, J. Kołodyński, A. Acín, and M. Lewenstein, "Random bosonic states for robust quantum metrology," Phys. Rev. X **6**, 041044 (2016).
[68]I. M. Georgescu, S. Ashhab, and F. Nori, "Quantum simulation," Rev. Mod. Phys. **86**, 153–185 (2014).
[69]G. Pelegrí, J. Mompart, and V. Ahufinger, "Quantum sensing using imbalanced counter-rotating Bose–Einstein condensate modes," New J. Phys. **20**, 103001 (2018).